

## ARTICLE OPEN



# Electrical switching of spin-polarized current in multiferroic tunneling junctions

Ligong Zhang<sup>1</sup>, Yuchen Wang<sup>1</sup>, Xiaoyan Liu<sup>1,2</sup> and Fei Liu<sup>1,2</sup>✉

The generation and manipulation of spin-polarized current are critical for spintronic devices. In this work, we propose a mechanism to generate and switch spin-polarized current by an electric field in multiferroic tunnel junctions (MFTJs), with symmetric interface terminations in an antiparallel magnetic state. In such devices, different spin tunneling barriers are realized by the magnetoelectric coupling effect, resulting in a spin-polarized current. By reversing the electric polarization of the ferroelectric layer, the spin polarization of current is efficiently switched for the exchange of spin tunneling barriers. By first-principles quantum transport calculations, we show that a highly spin-polarized current is obtained and manipulated by the electric field in hafnia-based MFTJs based on the proposed mechanism. We also demonstrate that four resistance states are realized in Co/HfO<sub>2</sub>/Co junctions with asymmetric interface terminations. This work provides a promising approach for realizing the electrical control of spin current for spintronic applications.

npj Computational Materials (2022)8:197; <https://doi.org/10.1038/s41524-022-00886-5>

## INTRODUCTION

Spintronic devices are promising for next-generation energy efficient computing, which utilize the spin degree of freedom of the electron for information storage and processing<sup>1–4</sup>. The generation of a pure spin-polarized current is one of the core technical challenges in developing spintronic applications<sup>1–4</sup>. The most common method to generate spin-polarized current is the application of magnetic fields or ferromagnetic (FM) materials<sup>5–10</sup>. Various spin-related fascinating effects, such as spin-optical effects<sup>11–15</sup>, spin-orbital effects<sup>16,17</sup>, and spin-caloritronic effects<sup>18–20</sup>, are applied to generate spin-polarized current. Manipulation of spin current is another fundamental challenge in spintronics<sup>1–4</sup>. The spin polarization is usually switched by a local magnetic field induced by a large current. However, such a conventional method is energetically unfavorable. It is necessary to realize a voltage control of spin currents for low power switching. The spin-orbit coupling provides additional possibilities to electrically control the spin-polarized current<sup>21–24</sup>, while it is a great challenge to realize a long spin coherence lifetime and strong spin-orbit coupling.

Strong magnetoelectric couplings can be achieved by engineering interfacial structures in multiferroic heterojunctions<sup>25,26</sup>. Therefore, there is a possibility of obtaining electrical control of magnetism by switching the direction of ferroelectric (FE) polarization at the interface between FM and FE layers<sup>27–31</sup>. The lattice strain or charge modulation induced by FE polarization switching can affect ferromagnetic moments at the interface of multiferroic heterostructures<sup>32,33</sup>. The ferroelectric control of interfacial magnetization can further change the tunnel magnetoresistance (TMR) in artificial MFTJs, such as Fe/BaTiO<sub>3</sub>/La<sub>1-x</sub>Sr<sub>x</sub>MnO<sub>3</sub> (LSMO)<sup>34</sup> and Co/Hf<sub>0.5</sub>Zr<sub>0.5</sub>O<sub>2</sub>/LSMO<sup>35</sup>. Moreover, multi-state storage can be achieved in MFTJs with a combination of FE and FM switching<sup>36–39</sup>.

In this work, we propose a mechanism to generate and switch the spin-polarized current in MFTJs. Symmetric interface terminations and antiparallel magnetic electrodes in MFTJs are applied to manipulate the spin-polarized tunnel current. Specifically, FE

hafnium oxide (HfO<sub>2</sub>) compatible with modern CMOS technology is applied as the tunneling barrier between the FM electrodes. First-principles quantum transport simulations show that highly spin-polarized currents can be generated and switched in Co/HfO<sub>2</sub>/Co junctions in an antiparallel state. We further explore interfacial effects on transport properties and demonstrate four resistance states in Co/HfO<sub>2</sub>/Co junctions.

## RESULTS

### The theory for ferroelectric control of spin current

An MFTJ has an ultrathin layer of FE insulator sandwiched between the two FM electrodes as shown in Fig. 1a, b. The FE polarization direction of the insulator can be switched from the right in Fig. 1a to the left in Fig. 1b by an electric field. The spin tunneling current through the device can be described by Julliere's model<sup>40</sup>:

$$J(E) \propto T_{\uparrow} DOS_1^{\uparrow} DOS_2^{\downarrow} + T_{\downarrow} DOS_1^{\downarrow} DOS_2^{\uparrow} \quad (1)$$

where,  $T_{\uparrow/\downarrow}$  is the tunneling probability of spin up/down state, and  $DOS_1$  and  $DOS_2$  indicate the density of states for the left and right electrodes, respectively. According to this model, spin tunneling probabilities should be switched to get an electrical control of spin current when the FE polarization direction is reversed in MFTJs. So, we propose MFTJs with symmetric interface terminations to switch the spin-polarization direction without changing the magnitude. There are four possible states depending on the electrodes' magnetic alignment ( $M_{\uparrow\uparrow}$  or  $M_{\uparrow\downarrow}$ ) and the FE polarization direction ( $P_{\rightarrow}$  or  $P_{\leftarrow}$ ) of the insulator. Figure 1c shows the schematic band profile of MFTJs at  $M_{\uparrow\uparrow}$  and  $P_{\rightarrow}$ . Spin states at the two interfaces of FE layers are split and the magnetization directions are the same due to the magnetic proximity effect with the parallel electrodes. Therefore, there are different spin tunnel barriers in Fig. 1c. In the reversal of FE polarization, spin tunnel barriers do not change, as shown Fig. 1d, and the spin-polarization direction of the tunneling current remains the same.

<sup>1</sup>School of Integrated Circuits, Peking University, 100871 Beijing, China. <sup>2</sup>Beijing Advanced Innovation Center for Integrated Circuits, 100871 Beijing, China.

✉email: feiliu@pku.edu.cn

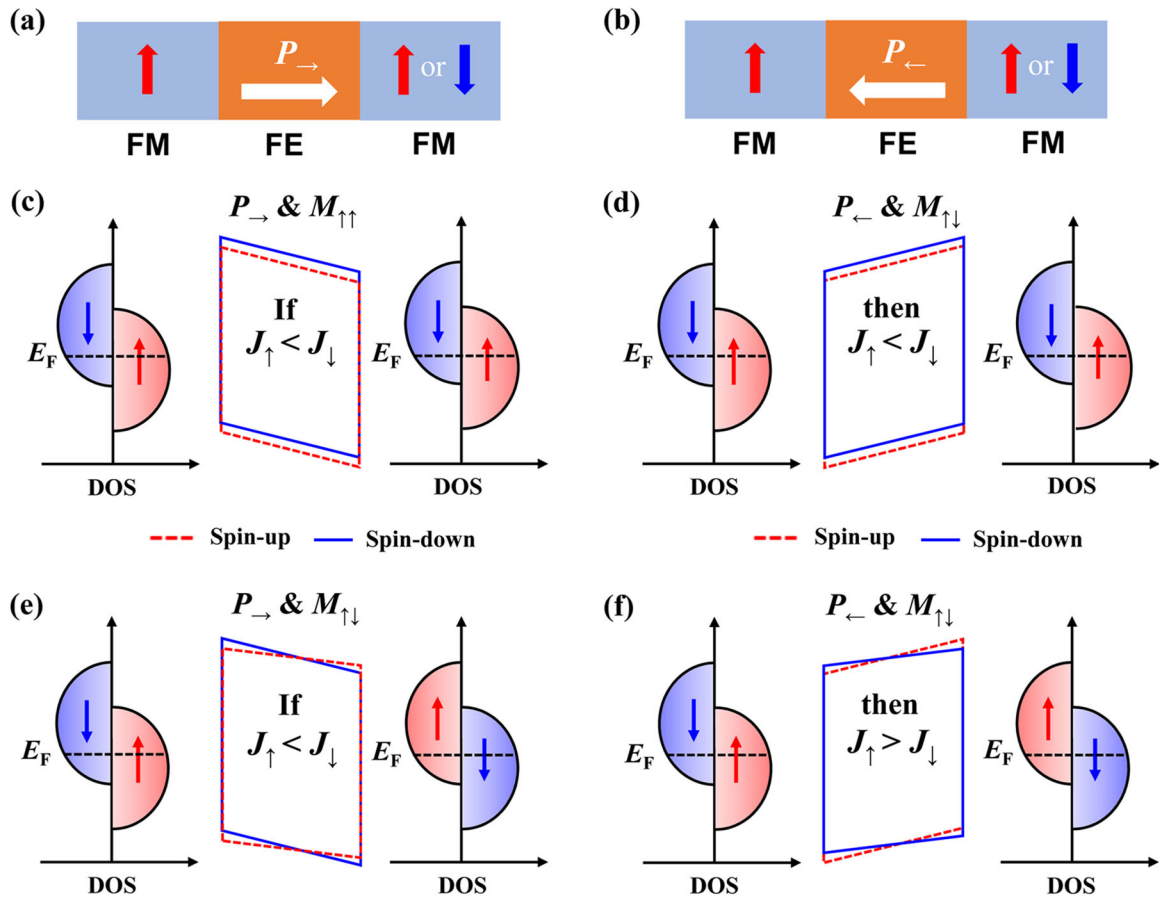


**Fig. 1** The schematic mechanism for generating and switching spin-polarized current in MFTJs. Device structures of MFTJs with a ferroelectric (FE) layer sandwiched between two ferromagnetic (FM) leads: (a) right and (b) left FE polarization. MFTJs with symmetric interface terminations and interfacial magnetization: (c)  $P_{\rightarrow}$  and (d)  $P_{\leftarrow}$  in a parallel magnetic state ( $M_{\uparrow\uparrow}$ ), (e)  $P_{\rightarrow}$  and (f)  $P_{\leftarrow}$  in an antiparallel magnetic state ( $M_{\uparrow\downarrow}$ ). The spin current polarization at  $M_{\uparrow\uparrow}$  does not change with the FE switching. If the current at  $P_{\rightarrow}$  and  $M_{\uparrow\uparrow}$  is spin-down polarized with  $J_{\uparrow} < J_{\downarrow}$ , the spin polarization direction of the tunnel current is switched with the reversal of FE polarization:  $J_{\uparrow} > J_{\downarrow}$  at  $P_{\leftarrow}$  and  $M_{\uparrow\uparrow}$ .

Therefore, spin polarization cannot be switched in MFTJs in a parallel state.

Next, we discuss the manipulation of the spin-polarized current in MFTJs in an antiparallel state. The magnetization directions at the two interfaces of FE layers are opposite due to the antiparallel magnetization of the two electrodes. The schematic band profile with oppositely magnetized interfaces is shown in Fig. 1e. Magnetization sequences and FE polarization result in different spin tunneling barriers with  $T_{\uparrow} \neq T_{\downarrow}$ , while  $DOS_{\uparrow}^1 DOS_{\downarrow}^1$  and  $DOS_{\uparrow}^2 DOS_{\downarrow}^2$  in Eq. (1) are the same in the antiparallel state. So, spin-polarized transport is realized in such junctions. The reverse of FE polarization can switch the spin tunnel barriers and change the spin-polarization direction of the tunnel current as shown in Fig. 1f. If the current is spin-down polarized at  $P_{\rightarrow}$  and  $M_{\uparrow\downarrow}$  as schematically shown in Fig. 1e, it gets spin-up polarized at  $P_{\leftarrow}$  and  $M_{\uparrow\downarrow}$ . Therefore, electrical control of spin-polarized current is realized in the proposed structure in an antiparallel state. In the following, MFTJs using FE  $\text{HfO}_2$  as the tunneling layer are constructed to realize electrical control of spin-polarized current according to the proposed mechanism.

### First-principles calculations

The FE phase of doped  $\text{HfO}_2$  thin films has recently been discovered<sup>41,42</sup>. Because of their compatibility with CMOS processes and their outstanding ferroelectricity at nanoscale thickness<sup>43–45</sup>,  $\text{HfO}_2$  has been the focus of extensive study. To realize the electrical control of spin current as discussed above,

MFTJs with cobalt electrodes and an  $\text{HfO}_2$  FE layer are constructed, as shown in Fig. 2a, b). The FE phase of orthorhombic structure  $Pca2_1$  is used as the insulator layer<sup>46–49</sup>. The in-plane lattice constants of the heterostructure are constrained to those of O-phase  $\text{HfO}_2$ , which corresponds to a strain of  $-2\%$  on cobalt electrodes. The relaxed lattice constants of O-phase  $\text{HfO}_2$  are 5.08 Å, 5.05 Å, and 5.27 Å in the unit vector directions, which agree with the experimental<sup>50,51</sup> and DFT<sup>52,53</sup> results.

The atomistic geometries of  $\text{HfO}_2$ -Co hetero-structures are optimized by the first-principles calculations using the Vienna Ab Initio Simulation Package (VASP)<sup>54–56</sup>. The distances between  $\text{HfO}_2$  and the cobalt electrodes are optimized, and central region atomistic structures are fully relaxed. The interfaces of Co/ $\text{HfO}_2$ /Co junctions terminated with Hf and O atoms are studied as shown in Fig. 2a, b. Hollow and top sites of Hf/O atoms on Co atoms are calculated. The atomistic structure with Hf/O atoms on the hollow sites has lower energy, consistent with the Ni/ $\text{HfO}_2$  interface<sup>57</sup>. The distances between Hf/O and Co atoms at the two interfaces are different due to oxygen displacement: about 2.2/0.9 Å and 1.9/1.3 Å for the left and right interfaces of the  $\text{HfO}_2$  thin film at  $D_{\leftarrow}$  ( $D_{\leftarrow}$  indicates the O atoms are displaced to the left), respectively. Robust ferroelectricity has been experimentally demonstrated in 1 nm HZO films grown on silicon<sup>45</sup>. So, 1 nm and 2 nm  $\text{HfO}_2$  films are considered in our calculations.

Oxygen atoms in  $Pca2_1$   $\text{HfO}_2$  can be classified into two types: one type of  $O_{\text{Sp}}$  belonging to the spacer layer and the other type of  $O_{\text{FE}}$  belonging to the FE layer<sup>48</sup>. The movement of  $O_{\text{FE}}$  atoms results in the FE switching of hafnia thin films. Hf-O displacements

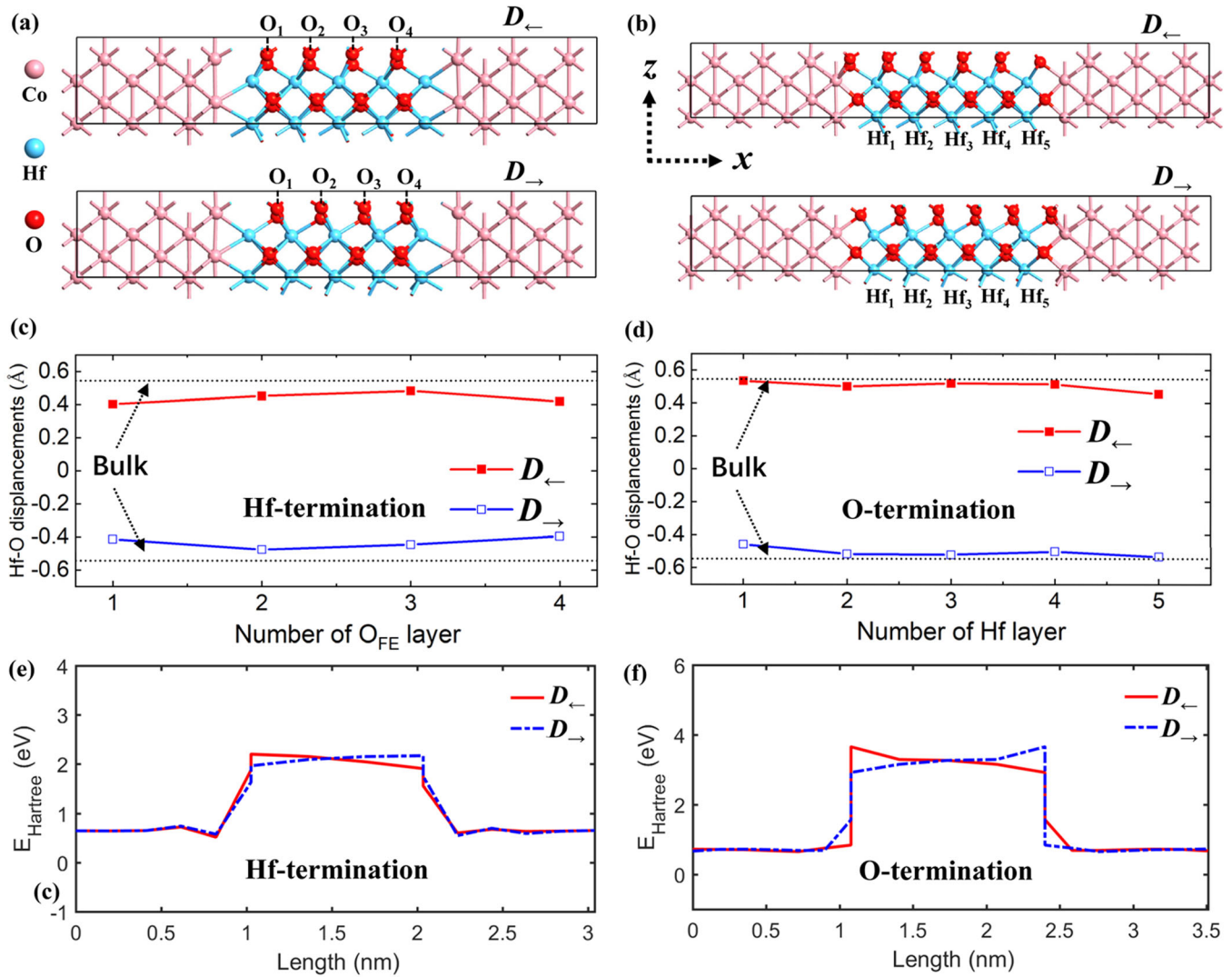


**Fig. 2** Atomistic structures, Hf-O displacements and Hartree potential energies of Co/HfO<sub>2</sub>/Co junctions. Atomistic structures of Co/HfO<sub>2</sub>/Co junctions in an antiparallel state with symmetric interfaces terminated by (a) Hf and (b) O atoms. The oxygen layers (O<sub>FE</sub>) responsible for the ferroelectricity are indicated in a. The Hf-O displacements across HfO<sub>2</sub> layers: (c) Hf-termination and (d) O-termination. The Hf-O displacement is calculated as the difference between the O<sub>FE</sub>/Hf coordinates along the x axis and the averaged x coordinate of the two adjacent Hf/O<sub>FE</sub> layers in the Hf/O-terminated case. The dashed line indicates the Hf-O displacement in bulk *Pca2<sub>1</sub>* HfO<sub>2</sub>. The calculated Hartree potential energies of Co/HfO<sub>2</sub>/Co junctions averaged in atomistic layers for *D*<sub>←</sub> and *D*<sub>→</sub> oxygen displacements: (e) Hf-terminated and (f) O-terminated cases.

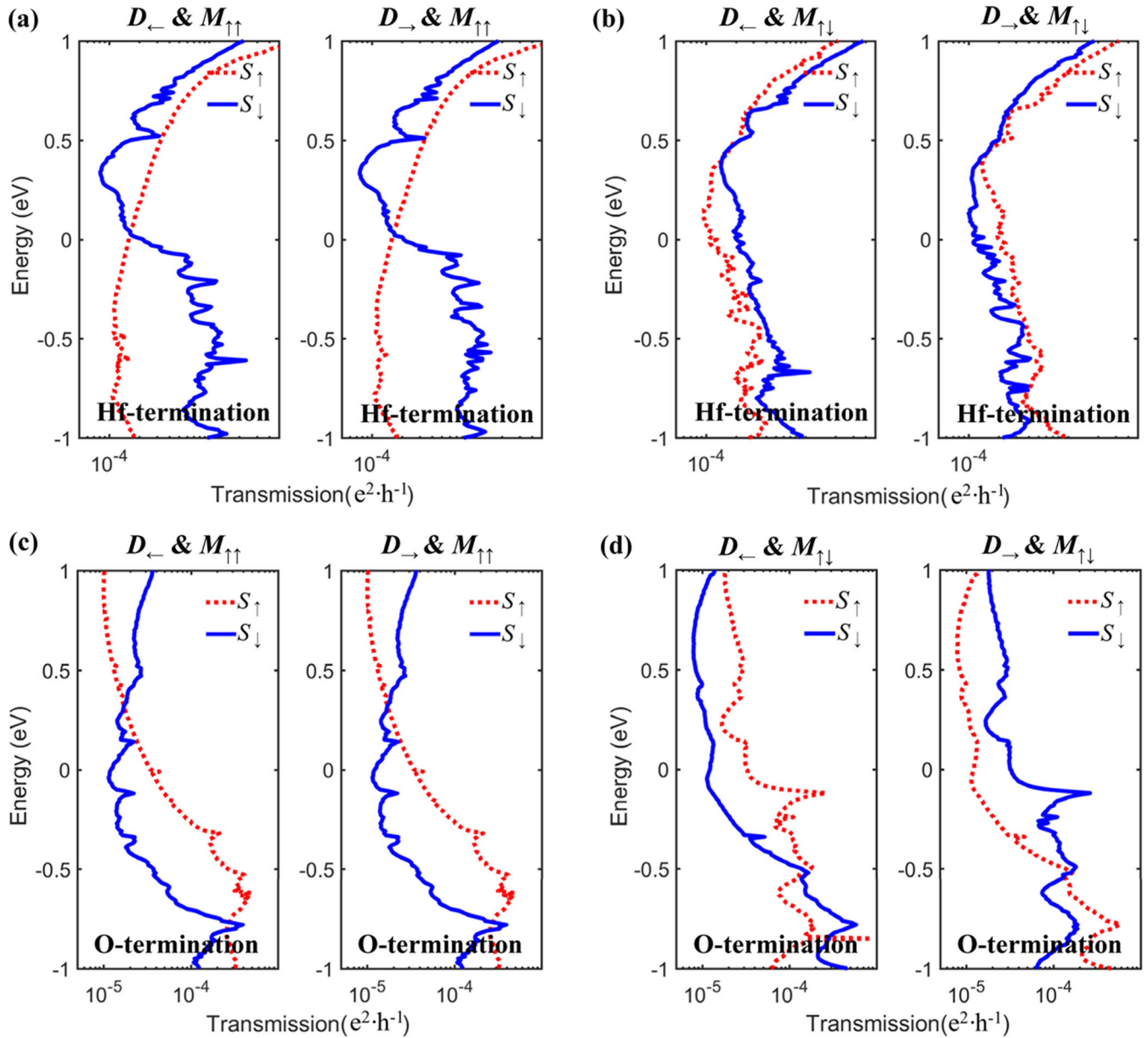
in Hf/O terminated HfO<sub>2</sub> thin films are given by the difference between the x coordinate of the O<sub>FE</sub>/Hf plane and the averaged x coordinate of the two adjacent Hf/O<sub>FE</sub> planes. The relative displacements between Hf and O<sub>FE</sub> atoms in the junctions are shown in Fig. 2c, d. Displacement magnitudes in the two HfO<sub>2</sub> thin films are smaller than that (0.54 Å) of bulk FE HfO<sub>2</sub>, and are reduced more significantly close to the interfaces of the Hf-terminated structure in Fig. 2c. Differently, only one side displacements are significantly reduced in the O-terminated structure in Fig. 2d.

Figure 2e, f show the calculated Hartree potential energies across junctions averaged within atomistic layers at the two FE polarization states. The electrostatic potentials are switched symmetrically due to the movement of oxygen atoms, which confirms the existence of ferroelectricity in HfO<sub>2</sub> thin film scaled to 1 nm<sup>45</sup>. When the HfO<sub>2</sub> layer is contacted with Co electrodes, additional screening charges appear at the interfaces. Because surface charges induced by the FE polarization cannot be fully screened, a sizeable depolarizing field exists in

Co/HfO<sub>2</sub>/Co junctions as shown in Fig. 2e, f. The magnitudes of the electric fields across the FE layer are about 2.9 MV·cm<sup>-1</sup> and 5.6 MV·cm<sup>-1</sup> for Hf and O terminated structures, respectively, which are more significant than that in BTO<sup>58</sup> and comparable with those experimental values in Hf<sub>0.5</sub>Zr<sub>0.5</sub>O<sub>2</sub><sup>59</sup> thin films and Y-doped bulk HfO<sub>2</sub><sup>60</sup>.

### Quantum transport simulations

Next, we study spin transport properties of Co/HfO<sub>2</sub>/Co junctions by first-principles quantum transport simulations<sup>61</sup>. Here, devices with symmetric interface terminations in Fig. 2a, b are investigated to obtain spin-polarized currents. Figure 3 shows transmissions as a function of energy for Hf-terminated and O-terminated cases. When the two electrodes are in a parallel magnetic state (*M*<sub>↑↑</sub>), spin-polarized states can be realized below the Fermi level *E*<sub>F</sub> = 0 eV in Fig. 3a, c. However, the tunnel barriers do not change for both spin up and down states when the FE polarization is reversed. Consequently, spin transmissions of *D*<sub>←</sub> and *D*<sub>→</sub> states are similar, as shown in Fig. 3a, c, for both Hf-terminated and



**Fig. 3 Spin dependent transmissions of Co/HfO<sub>2</sub>/Co junctions.** Transmission of Co/HfO<sub>2</sub>/Co junctions with symmetric interface terminations at different oxygen displacements ( $D$ ) and ferromagnetic ( $M$ ) polarization states: (a, b) the Hf-terminated structure, (c, d) the O-terminated structure.

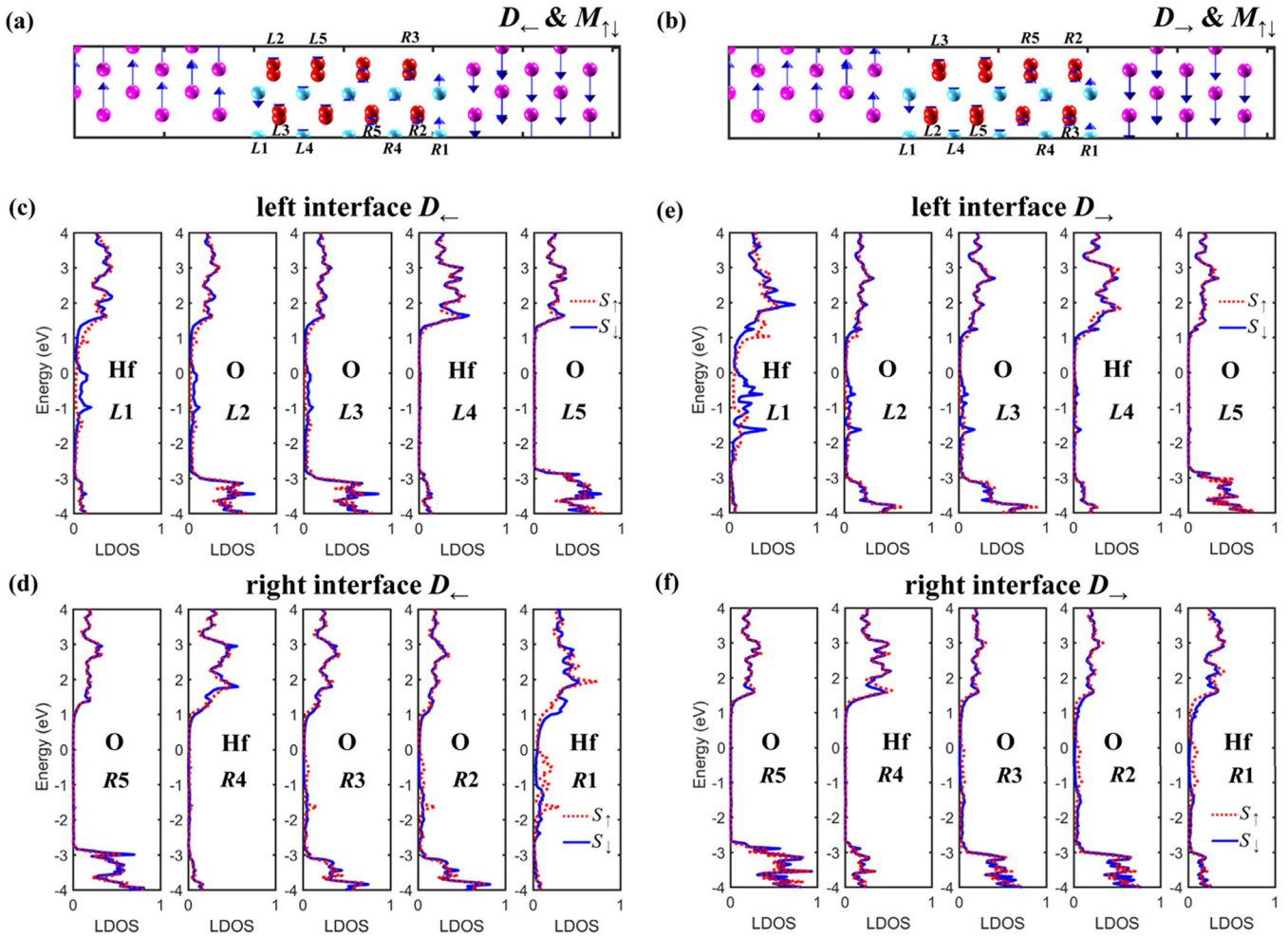
O-terminated junctions. Therefore, as expected, spin polarization cannot be changed by the FE switching in Co/HfO<sub>2</sub>/Co junctions in a parallel magnetic state.

Figure 3b, d also show spin transmissions of Co/HfO<sub>2</sub>/Co junctions in an anti-parallel magnetic state ( $M_{\uparrow\downarrow}$ ). It can be found that the tunnel currents through the junction are spin-polarized around the Fermi level for both Hf-terminated and O-terminated junctions. The current is mainly composed of spin-down carriers in the Hf-terminated junction at  $D_{\leftarrow}$  and  $M_{\uparrow\downarrow}$  as shown in Fig. 3b, while the current of the O-terminated junction is spin-up polarized at  $D_{\leftarrow}$  and  $M_{\uparrow\downarrow}$  as shown in Fig. 3d. Spin polarization is defined as  $P_s = (G_{\uparrow} - G_{\downarrow}) / (G_{\uparrow} + G_{\downarrow})$ , where  $G$  is spin-dependent conductance and can be calculated in the linear response regime as follows:

$$G_{\sigma} = \frac{e^2}{h} \int_{-\infty}^{+\infty} T_{\sigma}(E) \left( -\frac{\partial f}{\partial E} \right) dE \quad (2)$$

Where,  $T_{\sigma}(E)$  is the transmission at a given energy  $E$  with spin  $\sigma$ ,  $f$  is the Fermi-Dirac distribution function,  $h$  is the Plank constant, and  $e$  is the elementary charge.  $P_s$  of Co/HfO<sub>2</sub>/Co junctions at  $D_{\leftarrow}$  is about  $-30\%$  (spin-down polarized) and  $50\%$  (spin-up polarized) for Hf-terminated and O-terminated cases, respectively. As the oxygen displacement direction is reversed to  $D_{\rightarrow}$ , the current gets spin-up polarized with  $P_s$  around  $27\%$  for the Hf-terminated junction and spin-down polarized with  $P_s$  around  $-50\%$  for the O-terminated junction. Therefore, generation and manipulation of spin current are realized in Co/HfO<sub>2</sub>/Co junctions with symmetric interface terminations. The two electrodes' magnetization states are fixed, and the two leads' spin density of states in Eq. (1) do not change. Thus, the spin polarization switching can be attributed to the change of spin tunnel barriers across the FE HfO<sub>2</sub> layer due to orbital hybridization at the interfaces.

Figure 4 shows local magnetic moments and spin density of states (LSDOS) across the Co/HfO<sub>2</sub>/Co junctions with



**Fig. 4** Local magnetic moments and local density of states of Co/HfO<sub>2</sub>/Co junctions with Hf-terminated interfaces. Local magnetic moments of Co/HfO<sub>2</sub>/Co junctions with Hf-terminated interfaces at an antiparallel state: (a)  $D_{\leftarrow}$  and (b)  $D_{\rightarrow}$ . The five atomistic layers at the left and right interfaces are indicated. Layer dependent spin density of states of five atomistic layers at left and right interfaces of Co/HfO<sub>2</sub>/Co junctions with Hf-terminated interfaces: (c) the left interface and (d) the right interface at  $D_{\leftarrow}$ , (e) the left interface and (f) the right interface at  $D_{\rightarrow}$ .

Hf-terminated interfaces. Sizable magnetic moments are induced on the Hf ions at both interfaces in Fig. 4a, b, indicating hybridization of the orbitals between Co and Hf atoms<sup>38,62</sup>. Due to the displacement of oxygen atoms, the distance between Hf and Co atoms at the left interface of Co/HfO<sub>2</sub>/Co junctions at  $D_{\leftarrow}$  is larger than at the right interface. The larger orbital overlap between Hf and Co atoms enhances the induced moments on the Hf sites, resulting in different magnetic moments of Hf atoms in Fig. 4a: 0.29  $\mu_B$  and 0.37  $\mu_B$  for left and right interfaces, respectively, where  $\mu_B$  is the Bohr magneton. With the reversal of the FE polarization, magnetic moments of Hf atoms at left interfaces get larger than those at right interfaces due to the movement of oxygen atoms as shown in Fig. 4b. Figure 4a, b show that the local magnetic moments get smaller from the interface to the center of the FE layer. The calculated magnetic moments of Hf atoms at the left and right interfaces are opposite to those of the magnetic electrodes, consistent with the reversed spin polarization at the Co(001)-HfO<sub>2</sub>(001) interface<sup>62</sup>.

Figure 4 also depicts layer-dependent DOS at interfaces within five atomistic layers. The Hf atoms at interfaces have different DOS from those in bulk HfO<sub>2</sub>. At the left interface in Fig. 4c, there are more spin-down states around the Fermi level. Deeper into the center of the HfO<sub>2</sub> film, the DOS becomes spin degenerate like bulk HfO<sub>2</sub>. The HfO<sub>2</sub> film gets locally metallic within three atomic

layers at both left and right interfaces, and the rest layers are insulating (see the LSDOS across the junctions in Supplementary Fig. 1). While, DOS around the Fermi level are spin-up polarized at the right interface in Fig. 4d. As the FE polarization is reversed, the spin polarization directions at the two interfaces do not change as shown in Fig. 4e, f, which are fixed by the left and right leads. Spin-dependent transport properties of Co/HfO<sub>2</sub>/Co junctions with Hf-terminated interfaces can be understood from the LSDOS along the junction. From Fig. 4c, the conduction band edge of spin-up states has lower energy than that of spin-down states at the left interface when HfO<sub>2</sub> is at  $D_{\leftarrow}$ . While, the conduction band edge of spin-down states has lower energy than that of spin-up states at the right interface in Fig. 4d. Therefore, the conduction band edge at  $D_{\leftarrow}$  can be simplified as shown in Fig. 1e. Due to different spin tunneling barriers, the current through Co/HfO<sub>2</sub>/Co is spin-down polarized with  $T_{\uparrow} < T_{\downarrow}$  at  $E_F = 0$  eV as shown in Fig. 3a. When the oxygen displacement is reversed to  $D_{\rightarrow}$ , the tunnel barriers for spin-up and spin-down states are exchanged as shown in Fig. 4e, f, which is simplified in Fig. 1f. The spin-polarization of the tunneling current is switched with  $T_{\uparrow} > T_{\downarrow}$  at  $E_F = 0$  eV as shown in Fig. 3b. A similar discussion can also be performed for the spin current switching in O-terminated MFTJs in Fig. 3d.

We also study the transmission map in the 2D Brillouin zone and the real-space distribution of spin scattering states at

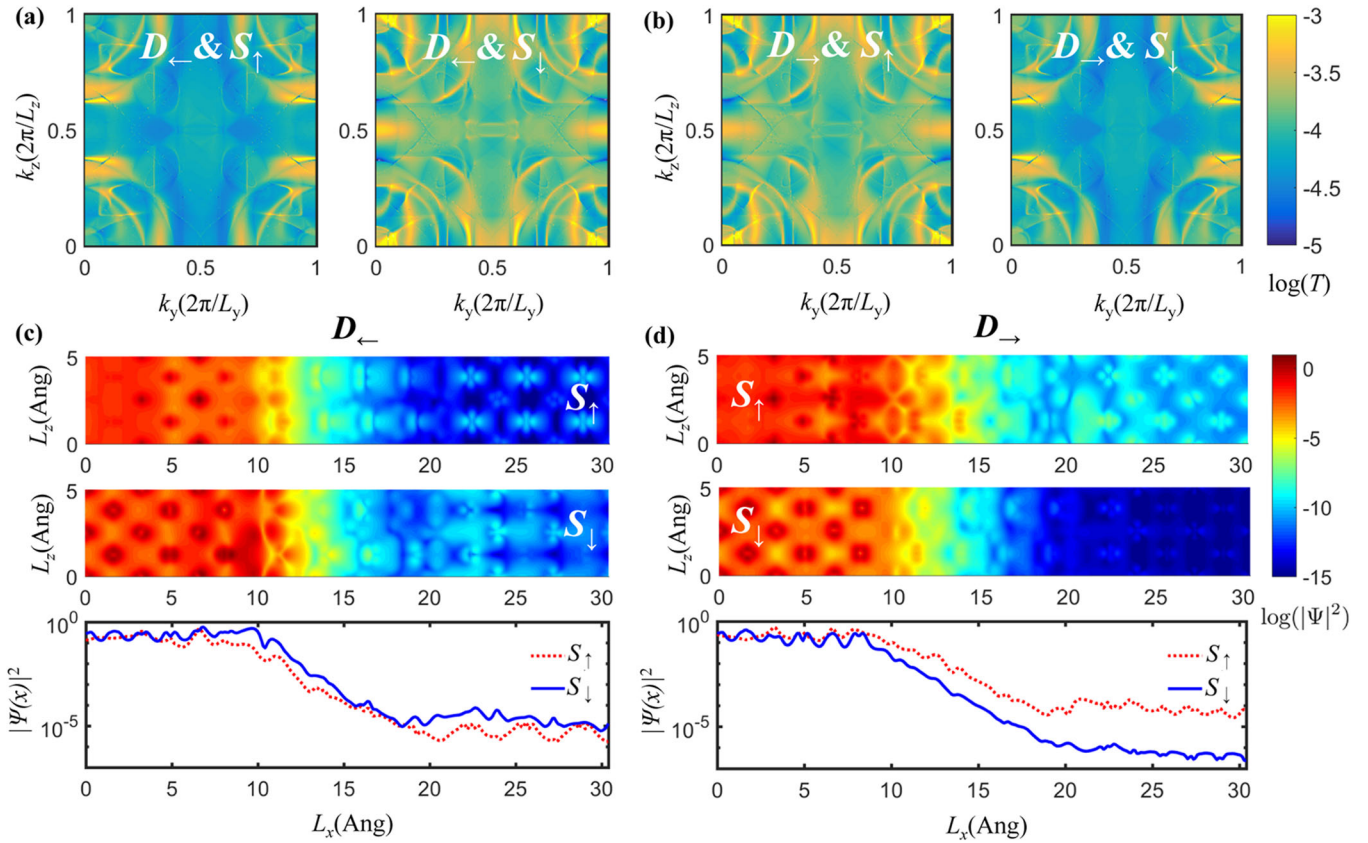


**Fig. 5 Spin dependent transmission maps, spin scattering states of the Co/HfO<sub>2</sub>/Co junction with Hf-terminated interfaces.** Spin dependent transmission maps in the 2D Brillouin zone of the Co/HfO<sub>2</sub>/Co junction with Hf-terminated interfaces at an antiparallel state at the Fermi level  $E = 0$  eV: (a)  $D_{\leftarrow}$  and (b)  $D_{\rightarrow}$ .  $S_{\uparrow}$  ( $S_{\downarrow}$ ) indicates spin-up (spin-down) state. Real space distribution of spin scattering states  $|\Psi(x, z)|^2$  and projected distribution of spin scattering states  $|\Psi(x)|^2$  at  $\mathbf{k}_t = (k_y, k_z) = (0, 0)$ : (c)  $D_{\leftarrow}$  and (d)  $D_{\rightarrow}$ .

$E_F = 0$  eV in Fig. 5. Figure 5a, b shows the transverse wave vector  $\mathbf{k}_t = (k_y, k_z)$  resolved transmission for spin-up and spin-down states at the Fermi level  $E_F = 0$  eV in the 2D Brillouin zone for two ferroelectric polarization orientations. It can be directly found that there are more spin-down tunnel channels at  $D_{\leftarrow}$  in Fig. 5a. With the reversal of ferroelectric polarization, there are more pronounced spin-up tunnel channels in Fig. 5b. Figure 5c, d plots spin scattering states in real space at  $\mathbf{k}_t = (k_y, k_z) = (0, 0)$ . Scattering states are eigenstates of the device structure<sup>61</sup>, which come from the left lead, tunnel through the insulator layer, and transmit into the right lead. Injected spin scattering states are the same and decay exponentially through the HfO<sub>2</sub> barrier for both FE polarization states as shown in Fig. 5c, d. It can be found that there is a longer decay length for the spin-up state at  $D_{\leftarrow}$  in Fig. 5c, while spin-down incoming states decay faster than spin-up states at  $D_{\rightarrow}$  in Fig. 5d. Therefore, spin polarization directions of out-coming scattering states are different due to the different interfacial properties: spin-down polarized at  $D_{\leftarrow}$  and spin-up polarized at  $D_{\rightarrow}$ . All these results manifest that generation and manipulation of spin current are realized in the proposed MFTJs.

In the proposed devices, the spin-polarized current is generated and switched by manipulating spin-dependent tunneling barriers due to interfacial magnetoelectric coupling. Therefore, it is critical to induce strong magnetoelectric coupling at interfaces to realize a high spin polarization. So, we study device structures with Hf atoms on top of Co atoms (see Supplementary Fig. 2a). The spin polarization ratio can be as high as  $-94\%$  at  $D_{\leftarrow}$  and is switched to  $94\%$  at  $D_{\rightarrow}$  (see Supplementary Fig. 2b), which manifests that the spin polarization properties of the proposed devices can be optimized by interfacial engineering.

### Spin detection

Figure 6 shows two device structures to detect the spin-polarized current generated by the proposed MFTJs. Each device structure consists of a spin generating part and a spin detecting part. The three layers on the left in Fig. 6a constitute an MFTJ to inject and manipulate the spin current. The whole device is in a low-resistance state when the spin-polarization direction of the injected current is parallel with the FM layer on the right, and transitions into a high-resistance state with the reversal of the FE polarization. The MFTJ in Fig. 6a works as a free FM layer in conventional MTJs, and the whole device is an FE-switching MTJ (FE-MTJ). It should be noted that the third layer on the left should be thinner than the spin diffusion length of cobalt because the spin current may decay due to momentum scattering in the FM layer. Figure 6b describes a nonlocal spin-valve device capable of detecting the spin current generated by the MFTJ. The spin current is injected from the two electrodes on the left and tunnels through the insulator to the normal metal. A nonlocal voltage would be detected between the two electrodes on the right due to the spin diffusion and accumulation. Such a device structure is beneficial for the detection of pure spin signals. In the two devices, no external magnetic field is required to switch the spin current polarization.

### Multistate properties

MFTJs combine the switching mechanisms of an MTJ and an FTJ and are promising for realizing multistate storage. Asymmetric interfaces are beneficial for enhancing tunneling electroresistance (TER)<sup>63,64</sup>. So, we construct MFTJs with one interface terminated

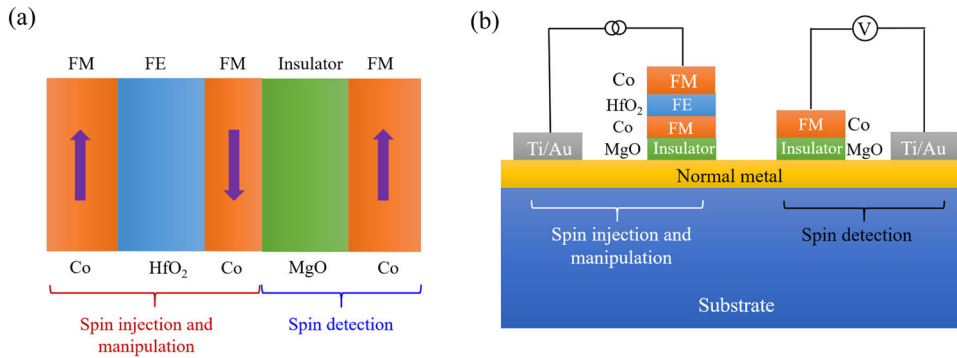


**Fig. 6 Schematic device structures for detecting the spin current generated by the proposed MFTJs. a** Ferroelectric switching MTJs (FE-MTJs): the left three layers constitute an MFTJ for spin generation and manipulation; the right two layers are for spin detection. The whole device is at a low-resistance/high-resistance state when the injected current is parallel/antiparallel with the far-right ferromagnetic layer. **b** Nonlocal spin valve for spin detection. Spin current is injected from the left two electrodes and is detected by the right two electrodes. The spin polarization direction of the injected current is switched with the reversal of ferroelectric polarization without a magnetic field.

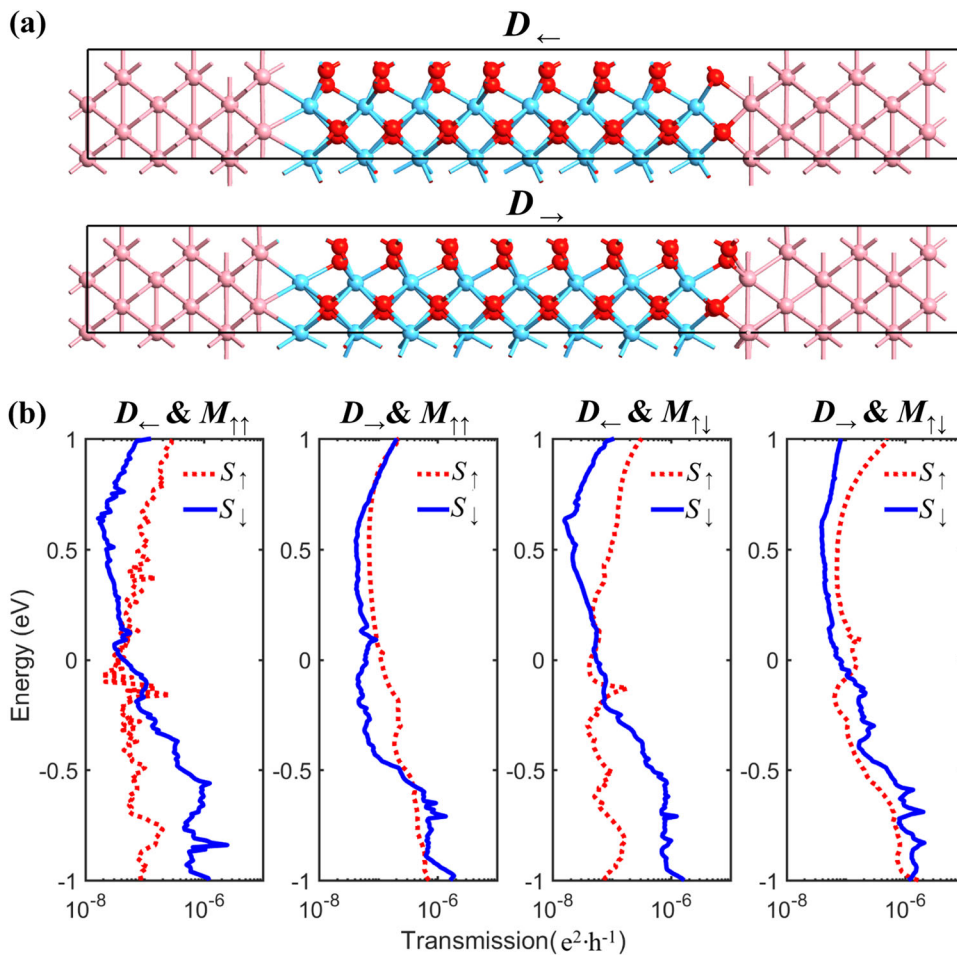


**Fig. 7 Atomistic structures and transmissions of the Co/HfO<sub>2</sub>/Co junction with asymmetric interface terminations. a** Atomistic structures and **(b)** transmissions of the Co/HfO<sub>2</sub>/Co junction with 2 nm HfO<sub>2</sub> and asymmetric interface terminations.

with Co-Hf and the other interface terminated with O-Co as shown in Fig. 7a. Due to the asymmetric interfaces, spin polarization is degraded and cannot be effectively modulated by switching the ferroelectric polarization direction of HfO<sub>2</sub> as shown in Fig. 7b. Spin polarization is 26% at  $D_{\rightarrow}$  and  $M_{\uparrow\downarrow}$ , and becomes  $-10\%$  at  $D_{\leftarrow}$  and  $M_{\uparrow\downarrow}$ . Multistate properties of the Co/HfO<sub>2</sub>/Co MFTJs are

summarized in Table 1. The TMR and TER ratios are defined as follows:

$$\text{TMR} = \frac{|(G_{\text{P}} - G_{\text{AP}})|}{\min(G_{\text{P}}, G_{\text{AP}})} \times 100\%, \quad \text{TER} = \frac{|(G_{\leftarrow} - G_{\rightarrow})|}{\min(G_{\leftarrow}, G_{\rightarrow})} \times 100\% \quad (3)$$

**Table 1.** Spin dependent conductance, TMR, TER and spin polarization ratio ( $P_s$ ) of the Co/HfO<sub>2</sub>/Co junction with 2 nm ferroelectric layer and asymmetric interface terminations at different oxygen displacements ( $D$ ) and ferromagnetic ( $M$ ) polarization states.

$G$ ( $\mu\text{S} \cdot \mu\text{m}^{-2}$ )	$M_{\uparrow\uparrow}$		$M_{\uparrow\downarrow}$		TMR (%)
	$G$	$P_s$	$G$	$P_s$	
$D_{\rightarrow}$	25.3	31%	32.0	26%	26%
$D_{\leftarrow}$	12.8	-12%	15.3	-10%	20%
TER (%)	98%		109%		

Where,  $G_P$  and  $G_{AP}$  are the conductances for parallel and antiparallel magnetization alignments, respectively.  $G_{\rightarrow}$  and  $G_{\leftarrow}$  are the conductances for the left and right oxygen displacements of the HfO<sub>2</sub> FE layer, respectively. Table 1 shows that the conductances of the Co/HfO<sub>2</sub>/Co junctions are modulated by electric and magnetic fields, which indicates the possibility of realizing multilevel information storage. TER can be over 98% for both parallel and antiparallel magnetization states by reversing the FE polarization, while TMR is 20% and 26% for the left and right oxygen displacements, respectively.

## DISCUSSION

In conclusion, we have proposed a mechanism to generate and switch spin-polarized current in multiferroic tunnel junctions with symmetric interface terminations. Different spin tunneling barriers in the FE layer are induced by interfacial magnetoelectric coupling with leads at antiparallel magnetization and can be exchanged by the FE switching. Specifically, spin current generation and manipulation are explored in Co/HfO<sub>2</sub>/Co junctions by quantum transport simulations. It is demonstrated that a highly spin-polarized current can be achieved and switched in Co/HfO<sub>2</sub>/Co junctions. Furthermore, four states can be realized by constructing asymmetric interfaces. The proposed mechanism is general and can be applied to generate and manipulate spin current using other materials, such as emerging two-dimensional materials. Our work offers design principles for realizing electric field switchable spin current in multiferroic heterostructures for spintronic applications.

## METHODS

### First-principles simulations

Atomic structures of Co/HfO<sub>2</sub>/Co junctions are calculated with the projector augmented wave (PAW) method as implemented in the Vienna Ab Initio Simulation Package (VASP)<sup>54–56</sup>. The generalized gradient approximation (GGA) of Perdew–Burke–Ernzerhof (PBE) type<sup>65</sup> is used for the exchange correlation functional in all calculations. An energy cutoff of the plane wave basis is set at 550 eV. The interface distances between the two Co leads and ferroelectric HfO<sub>2</sub> layer are first optimized. Then, the hafnium oxide layer and over six atomic layers of the left and right Co leads are fully relaxed. Atomic relaxations are performed using a  $1 \times 6 \times 6$   $k$ -point mesh for the Brillouin zone sampling until the forces were smaller than  $0.02 \text{ eV} \cdot \text{\AA}^{-1}$ . In the constructed hetero-junctions, the in-plane lattice constants are fixed as the calculated value of O-phase HfO<sub>2</sub>, and strain is applied on cobalt electrodes.

### Quantum transport calculations

First-principles quantum transport calculations are based on real-space density functional theory (DFT) within the Keldysh nonequilibrium Green's functions (NEGF) formalism, as implemented in

the nanocal package<sup>61</sup>. A double zeta polarized (DZP) atomic orbital basis set is applied to expand all the physical quantities. The exchange and correlation potential are treated with PBE-GGA. An equivalent energy cutoff of 200 Ry (1 Ry = 13.6 eV). A  $1 \times 6 \times 6$   $k$ -point mesh is used for self-consistent calculations of Co/HfO<sub>2</sub>/Co junctions.  $K$ -point mesh of  $1 \times 40 \times 40$  is used for calculating the transmission coefficient.

## DATA AVAILABILITY

The data that support the findings of this study are available from the corresponding author upon reasonable request.

Received: 20 February 2022; Accepted: 4 September 2022;

Published online: 16 September 2022

## REFERENCES

- Žutić, I., Fabian, J. & Das Sarma, S. Spintronics: fundamentals and applications. *Rev. Mod. Phys.* **76**, 323 (2004).
- Chappert, C., Fert, A. & Van Dau, F. N. The emergence of spin electronics in data storage. *Nat. Mater.* **6**, 813 (2007).
- Awschalom, D. D. & Flatte, M. E. Challenges for semiconductor spintronics. *Nat. Phys.* **3**, 153 (2007).
- Bader, S. D. & Parkin, S. S. P. Spintronics. *Annu. Rev. Condens. Matter Phys.* **1**, 71 (2010).
- Fiederling, R. et al. Injection and detection of a spin-polarized current in a light-emitting diode. *Nature* **402**, 787 (1999).
- Zhu, H. J. et al. Room-temperature spin injection from Fe into GaAs. *Phys. Rev. Lett.* **87**, 016601 (2001).
- Jiang, X. et al. Highly spin-polarized room-temperature tunnel injector for semiconductor spintronics using MgO (100). *Phys. Rev. Lett.* **94**, 056601 (2005).
- Dash, S. P., Sharma, S., Patel, R. S., de Jong, M. P. & Jansen, R. Electrical creation of spin polarization in silicon at room temperature. *Nature* **462**, 491 (2009).
- Dong, X. Y. Spin injection from the Heusler alloy Co<sub>2</sub>MnGe into Al<sub>0.1</sub>Ga<sub>0.9</sub>As/GaAs heterostructures. *Appl. Phys. Lett.* **86**, 102107 (2005).
- Ramsteiner, M. et al. Co<sub>2</sub>FeSi/GaAs/(Al,Ga)As spin light-emitting diodes: competition between spin injection and ultrafast spin alignment. *Phys. Rev. B* **78**, 121303 (2008).
- Kroutvar, M. et al. Optically programmable electron spin memory using semiconductor quantum dots. *Nature* **432**, 81 (2004).
- Urbaszek, B. et al. Efficient dynamical nuclear polarization in quantum dots: temperature dependence. *Phys. Rev. B* **76**, 201301 (2007).
- Zeng, H., Dai, J., Yao, W., Xiao, D. & Cui, X. Valley polarization in MoS<sub>2</sub> monolayers by optical pumping. *Nat. Nanotechnol.* **7**, 490 (2012).
- Zhu, B., Zeng, H., Dai, J., Gong, Z. & Cui, X. Anomalous robust valley polarization and valley coherence in bilayer WS<sub>2</sub>. *Proc. Natl Acad. Sci. USA* **111**, 11606 (2014).
- Huang, Y. et al. Room-temperature electron spin polarization exceeding 90% in an opto-spintronic semiconductor nanostructure via remote spin filtering. *Nat. Photonics* **15**, 475 (2021).
- Manchon, A., Koo, H. C., Nitta, J., Frolov, S. M. & Duine, R. A. New perspectives for Rashba spin-orbit coupling. *Nat. Mater.* **14**, 871 (2015).
- Sinova, J., Valenzuela, S. O., Wunderlich, J., Back, C. H. & Jungwirth, T. Spin hall effects. *Rev. Mod. Phys.* **87**, 1213 (2015).
- Uchida, K. et al. Observation of the spin Seebeck effect. *Nature* **455**, 7214 (2008).
- Slachter, A., Bakker, F. L., Adam, J.-P. & van Wees, B. J. Thermally driven spin injection from a ferromagnet into a non-magnetic metal. *Nat. Phys.* **6**, 882 (2010).
- Adachi, H., Uchida, K., Saitoh, E. & Maekawa, S. Theory of the spin Seebeck effect. *Rep. Prog. Phys.* **76**, 036501 (2013).
- Miron, I. M. et al. Current-driven spin torque induced by the Rashba effect in a ferromagnetic metal layer. *Nat. Mater.* **9**, 230 (2010).
- Miron, I. M. et al. Perpendicular switching of a single ferromagnetic layer induced by in-plane current injection. *Nature* **476**, 189 (2011).
- Liu, L., Lee, O. J., Gudmundsen, T. J., Ralph, D. C. & Buhrman, R. A. Current-induced switching of perpendicularly magnetized magnetic layers using spin torque from the Spin Hall effect. *Phys. Rev. Lett.* **109**, 096602 (2012).
- Liu, L. Q. et al. Spin-torque switching with the giant Spin Hall effect of Tantalum. *Science* **336**, 555 (2012).
- Vaz, C. A. F. Electric field control of magnetism in multiferroic heterostructures. *J. Phys. Condens. Matter* **24**, 333201 (2012).
- Matsukura, F., Tokura, Y. & Ohno, H. Control of magnetism by electric fields. *Nat. Nanotech.* **10**, 209 (2015).

27. Duan, C., Jaswal, S. S. & Tsymbal, E. Y. Predicted magnetoelectric effect in Fe/BaTiO<sub>3</sub> multilayers: ferroelectric control of magnetism. *Phys. Rev. Lett.* **97**, 047201 (2006).
28. Garcia, V. et al. Ferroelectric control of spin polarization. *Science* **327**, 1106 (2010).
29. Vaz, C. A. F., Hoffman, J., Ahn, C. H. & Ramesh, R. Magnetoelectric coupling effects in multiferroic complex oxide composite structures. *Adv. Mater.* **22**, 2900 (2010).
30. Pantel, D., Goetze, S., Hesse, D. & Alexe, M. Reversible electrical switching of spin polarization in multiferroic tunnel junctions. *Nat. Mater.* **11**, 289 (2012).
31. Radaelli, G. et al. Electric control of magnetism at the Fe/BaTiO<sub>3</sub> interface. *Nat. Commun.* **5**, 3404 (2014).
32. Vaz, C. A. F. et al. Origin of the magnetoelectric coupling effect in Pb(Zr<sub>0.2</sub>Ti<sub>0.8</sub>)O<sub>3</sub>/La<sub>0.85</sub>Sr<sub>0.2</sub>MnO<sub>3</sub> multiferroic heterostructures. *Phys. Rev. Lett.* **104**, 127202 (2010).
33. Lu, H. et al. Electric modulation of magnetization at the BaTiO<sub>3</sub>/La<sub>0.67</sub>Sr<sub>0.33</sub>MnO<sub>3</sub> interfaces. *Appl. Phys. Lett.* **100**, 232904 (2012).
34. Valencia, S. et al. Interface-induced room-temperature multiferroicity in BaTiO<sub>3</sub>. *Nat. Mater.* **10**, 753 (2011).
35. Wei, Y. et al. Magneto-ionic control of spin polarization in multiferroic tunnel junctions. *npj Quantum Mater.* **4**, 62 (2019).
36. Garcia, V. & Bibes, M. Ferroelectric tunnel junctions for information storage and processing. *Nat. Commun.* **5**, 4289 (2014).
37. Velev, J. P. et al. Magnetic tunnel junctions with ferroelectric barriers: prediction of four resistance States from first principles. *Nano Lett.* **9**, 427 (2009).
38. Borisov, V. S., Ostanin, S., Maznichenko, I. V., Ernst, A. & Mertig, I. Magnetoelectric properties of the Co/PbZr<sub>x</sub>Ti<sub>1-x</sub>O<sub>3</sub> (001) interface studied from first principles. *Phys. Rev. B* **89**, 054436 (2014).
39. Tornos, J. et al. Ferroelectric control of interface spin filtering in multiferroic tunnel junctions. *Phys. Rev. Lett.* **122**, 037601 (2019).
40. Julliere, M. Tunneling between ferromagnetic films. *Phys. Lett. A* **54**, 225 (1975).
41. Boscke, T. S., Muller, J., Brauhaus, D., Schroder, U. & Bottger, U. Ferroelectricity in hafnium oxide thin films. *Appl. Phys. Lett.* **99**, 102903 (2011).
42. Müller, J. et al. Ferro-electricity in simple binary ZrO<sub>2</sub> and HfO<sub>2</sub>. *Nano Lett.* **12**, 4318 (2012).
43. Tian, X. et al. Evolution of ferroelectric HfO<sub>2</sub> in ultrathin region down to 3 nm. *Appl. Phys. Lett.* **112**, 102902 (2018).
44. Chernikova, A. et al. Ultrathin Hf<sub>0.5</sub>Zr<sub>0.5</sub>O<sub>2</sub> ferroelectric films on Si. *ACS Appl. Mater. Interfaces* **8**, 7232 (2016).
45. Cheema, S. S. et al. Enhanced ferroelectricity in ultrathin films grown directly on silicon. *Nature* **580**, 478 (2020).
46. Huan, T. D., Sharma, V., Rossetti, G. A. & Ramprasad, R. Pathways towards ferroelectricity in hafnia. *Phys. Rev. B* **90**, 064111 (2014).
47. Materlik, R., Künneth, C. & Kersch, A. The origin of ferroelectricity in Hf<sub>1-x</sub>Zr<sub>x</sub>O<sub>2</sub>: a computational investigation and a surface energy model. *J. Appl. Phys.* **117**, 134109 (2015).
48. Lee, H.-J. et al. Scale-free ferroelectricity induced by flat phonon bands in HfO<sub>2</sub>. *Science* **369**, 1343 (2020).
49. Qi, Y. & Rabe, K. M. Phase competition in HfO<sub>2</sub> with applied electric field from first principles. *Phys. Rev. B* **102**, 214108 (2020).
50. Suyama, R., Takubo, H. & Kume, S. Synthesis of Hf<sub>1-x</sub>Zr<sub>x</sub>O<sub>2</sub>. *J. Am. Ceram. Soc.* **68**, C237 (1985).
51. Sang, X., Grimley, E. D., Schenk, T., Schroeder, U. & LeBeau, J. M. On the structural origins of ferroelectricity in HfO<sub>2</sub> thin films. *Appl. Phys. Lett.* **106**, 162905 (2015).
52. Huan, T. D., Sharma, V., Rossetti, G. A. & Ramprasad, R. Pathways towards ferroelectricity in hafnia. *Phys. Rev. B* **90**, 064111 (2014).
53. Materlik, R., Künneth, C. & Kersch, A. The origin of ferroelectricity in Hf<sub>1-x</sub>Zr<sub>x</sub>O<sub>2</sub>: a computational investigation and a surface energy model. *J. Appl. Phys.* **117**, 134109 (2015).
54. Kresse, G. & Hafner, J. Ab initio molecular dynamics for liquid metals. *Phys. Rev. B* **47**, 558 (1993).
55. Kresse, G. & Furthmüller, J. Efficient iterative schemes for ab initio total-energy calculations using a plane-wave basis set. *Phys. Rev. B* **54**, 11169 (1996).
56. Kresse, G. & Furthmüller, J. Efficiency of ab-initio total energy calculations for metals and semiconductors using a plane-wave basis set. *Comput. Mater. Sci.* **6**, 15 (1996).
57. Yang, Q. et al. Magnetoelectric effect at the Ni/HfO<sub>2</sub> interface induced by ferroelectric polarization. *Phys. Rev. Appl.* **12**, 024044 (2019).
58. Junquera, J. & Ghosez, P. Critical thickness for ferroelectricity in perovskite ultrathin films. *Nature* **422**, 506 (2003).
59. Lyu, J., Fina, I., Solanas, R., Fontcuberta, J. & Sánchez, F. Growth window of ferroelectric epitaxial Hf<sub>0.5</sub>Zr<sub>0.5</sub>O<sub>2</sub> Thin Films. *ACS Appl. Electron. Mater.* **1**, 220 (2019).
60. Xu, X. et al. Kinetically stabilized ferroelectricity in bulk single-crystalline HfO<sub>2</sub>:Y. *Nat. Mater.* **20**, 826–832 (2021).
61. Taylor, J., Guo, H. & Wang, J. Ab initio modeling of quantum transport properties of molecular electronic devices. *Phys. Rev. B* **63**, 245407 (2001).
62. de Boer, P. K., de Wijs, G. A. & de Groot, R. A. Reversed spin polarization at the Co(001)-HfO<sub>2</sub>(001) interface. *Phys. Rev. B* **58**, 15422 (1998).
63. Velev, J. P., Burton, J. D., Zhuravlev, M. Y. & Tsymbal, E. Y. Predictive modelling of ferroelectric tunnel junctions. *npj Comput. Mater.* **2**, 16009 (2016).
64. Seo, J. & Shin, M. Atomistic asymmetric effect on the performance of HfO<sub>2</sub>-based ferroelectric tunnel junctions. *Phys. Rev. Appl.* **14**, 054018 (2020).
65. Perdew, J. P., Burke, K. & Ernzerhof, M. Generalized gradient approximation made simple. *Phys. Rev. Lett.* **77**, 3865 (1996).

## ACKNOWLEDGEMENTS

This work was supported by the National Key Research and Development Program of China under Grant 2019YFB2205100, the National Natural Science Foundation of China under Grant 61974003 and the 111 Project (B18001). We thank high-performance computing platform of Peking University for computation facilities.

## AUTHOR CONTRIBUTIONS

F.L. conceived and supervised the project. F.L. and L.Z. performed device simulations. F.L. wrote the manuscript. All the authors discussed the results and commented on the manuscript.

## COMPETING INTERESTS

The authors declare no competing interests.

## ADDITIONAL INFORMATION

**Supplementary information** The online version contains supplementary material available at <https://doi.org/10.1038/s41524-022-00886-5>.

**Correspondence** and requests for materials should be addressed to Fei Liu.

**Reprints and permission information** is available at <http://www.nature.com/reprints>

**Publisher's note** Springer Nature remains neutral with regard to jurisdictional claims in published maps and institutional affiliations.



**Open Access** This article is licensed under a Creative Commons Attribution 4.0 International License, which permits use, sharing, adaptation, distribution and reproduction in any medium or format, as long as you give appropriate credit to the original author(s) and the source, provide a link to the Creative Commons license, and indicate if changes were made. The images or other third party material in this article are included in the article's Creative Commons license, unless indicated otherwise in a credit line to the material. If material is not included in the article's Creative Commons license and your intended use is not permitted by statutory regulation or exceeds the permitted use, you will need to obtain permission directly from the copyright holder. To view a copy of this license, visit <http://creativecommons.org/licenses/by/4.0/>.

© The Author(s) 2022